TOPOLOGICAL OPTICS

Four-dimensional conserved topological charge vectors in plasmonic quasicrystals

Shai Tsesses[1,2], Pascal Dreher[3], David Janoschka[3], Alexander Neuhaus[3], Kobi Cohen[1], Tim C. Meiler[4,5], Tomer Bucher[1], Shay Sapir[1,6], Bettina Frank[4], Timothy J. Davis[3,4,7], Frank Meyer zu Heringdorf[3], Harald Giessen[4], Guy Bartal[1]*

According to Noether's theorem, symmetries in a physical system are intertwined with conserved quantities. These symmetries often determine the system topology, which is made ever more complex with increased dimensionality. Quasicrystals have neither translational nor global rotational symmetry, yet they intrinsically inhabit a higher-dimensional space in which symmetry resurfaces. Here, we discovered topological charge vectors in four dimensions (4D) that govern the real-space topology of 2D quasicrystals and reveal their inherent conservation laws. We demonstrate control over the topology in pentagonal plasmonic quasilattices, mapped by both phase-resolved and time-domain near-field microscopy, showing that their temporal evolution continuously tunes the 2D projections of their distinct 4D topologies. Our work provides a route to experimentally probe the thermodynamic properties of quasicrystals and topological physics in 4D and above.

Topology is the study of geometrical objects and their conserved properties under continuous deformation such as stretching, twisting, and bending. The values of conserved properties, often referred to as topological charges, can have a profound influence on the behavior of the system, from the formation of cosmic objects (1) to the dislocations of simple wave interference (2). Topological analysis has been especially impactful in the fields of condensed matter physics and optics, revealing robust transport phenomena (3, 4) and exotic phase transitions (5, 6) because of the existence of a topological charge in energy-momentum space known as the Chern number (7). Conversely, real-space topological charges can be used to control the way that light interacts with matter (8, 9) or may represent digital information for storage, processing, and transfer (10, 11).

Dimensionality greatly influences the topology and subsequent topological charges of a physical system (12–14), producing a larger variety of phenomena as it increases (15–17). The search for more complex topologies in a given physical system led to methods for artificially increasing system dimensionality (18–20), creating the field of physics in synthetic dimensions (21). By contrast, quasicrystalline systems (22, 23) can naturally have higher-dimensional topologies (24), resulting in the generation of topological charge vectors, as was previously observed in the band structure of atomic (25) and optical (26) systems.

Because quasicrystals have additional degrees of freedom compared with ordinary periodic structures, they behave as regular crystals but in a higher-dimensional plane (27–29). Thus, the topology in this higher-dimensional plane should affect the real-space structure of quasicrystals, making them an ideal platform with which to examine topological physics in higher dimensions. However, because topology is closely linked with the symmetry of the system (30), and quasicrystals lack translational or global rotational symmetry in the physical plane, the challenge of identifying and observing their topological charges in real space remains.

High-dimensional dislocations determine the topology of quasicrystals

We start by reviewing the relationship between topological charges and dislocations. The topology of the parameter space associated with a physical system can be determined by mapping the changes in the physical parameters along a closed loop in real space (31). For example, a wave exhibiting orbital angular momentum forms a vortex with a phase singularity at its center, which represents a defect also known as a dislocation in the parameter space (i.e., the phase of the wave). By mapping the change in phase along a loop enclosing the singularity, completing the loop accumulates a total phase that is an integer multiple q of 2π. The integer q characterizes the topological charge of the vortex (32), denoting the number of times that the phase completes a unit circle along the loop.

The same dislocation can also be described from another perspective: To return to the starting phase, one needs to subtract $b = 2\pi q$, which can be thought of as a one-dimensional (1D) vector. Extending this concept to many dimensions results in dislocation vectors that in turn can give rise to topological charge vectors. This point of view is common in crystallography, where a displacement vector in the crystal, the Burgers vector, defines the existing dislocation and the underlying topology of the crystal (31). There is some similarity between the dislocations in a crystal and those in a wave vortex, because summing over the atomic lattice vectors while traversing in a closed loop about the crystal dislocation gives a nontrivial (nonzero) outcome. We will show how dislocations hold the key to understanding the topological charges of quasicrystals, which naturally exhibit higher-dimensional behavior.

Quasicrystals can be represented as a superposition of waves with different phases (27–29), from which one can deduce the form of the possible dislocations. This work focuses on pentagonal crystals (33–35), the simplest 2D quasicrystals created by five waves interfering in a plane (Fig. 1C) and represented by the function

$$f(\vec{r}) = \text{Re} \sum_{m=1}^{5} |f_m| e^{i\phi_m} e^{i\vec{k}_m \cdot \vec{r}} \quad (1)$$

where $|f_m|$, ϕ_m, and $\vec{k}_m$ are the amplitude, relative phase, and wave vector of every wave in the interference pattern, respectively, and $\vec{r}$ is an in-plane position vector. This description is valid for any pentagonal system provided that one considers only low-order excitations, wherein the sum of phases $\Gamma = \sum_{m=1}^{5} \phi_m$ is constant up to integers of 2π and $\sum_{m=1}^{5} \vec{k}_m = 0$ (28, 36) (i.e., the wave vectors span a regular pentagon).

Consequently, the form of the dislocation vector associated with defects in the quasicrystal, $\vec{b} = ([b_1, b_2], [b_3, b_4]) = (\vec{b}_{phonon}, \vec{b}_{phason})$, also known as the Burgers vector (37), can be constructed solely from the four remaining independent relative phases ϕ_n (28, 29, 36) as follows:

$$\phi_n = \vec{k}_n \cdot \vec{b}_{phonon} + \frac{\sin(2\pi/5)}{\sin(4\pi/5)} \vec{k}_{\text{mod}(3n,5)}$$
$$\cdot \vec{b}_{phason} + \frac{\Gamma}{5} \quad (2)$$

where n is an integer with the possible values $n = \{1,...,4\}$. The system of equations in Eq. 2 implies that $\vec{b}_{phonon}$ represents displacements in the physical 2D space known as phonons, and $\vec{b}_{phason}$ represents displacements in two additional degrees of freedom called phasons.

[1]Andrew and Erna Viterbi Department of Electrical and Computer Engineering, Technion – Israel Institute of Technology, Haifa, Israel. [2]Department of Physics, MIT-Harvard Center for Ultracold Atoms and Research Laboratory of Electronics, Massachusetts Institute of Technology, Cambridge, MA, USA. [3]Faculty of Physics and Center for Nanointegration, Duisburg-Essen (CENIDE), University of Duisburg-Essen, Duisburg, Germany. [4]4th Physics Institute, Research Center SCoPE, and Integrated Quantum Science and Technology Center, University of Stuttgart, Stuttgart, Germany. [5]Centre for Disruptive Photonic Technologies and School of Physical and Mathematical Sciences, Nanyang Technological University, Singapore, Singapore. [6]Faculty of Mathematics and Computer Science, Weitzmann Institute of Science, Rehovot, Israel. [7]School of Physics, University of Melbourne, Parkville, Victoria, Australia.
*Corresponding author. Email: guy@ee.technion.ac.il

Fig. 1. Studying dislocations in quasicrystals and their resultant topological charges: Concept and implementation.
(**A**) Close to their ground state, quasicrystals in pentagonal symmetry can be described by the interference of five waves, oriented at angles that are integer multiples of $2\pi/5$. (**B**) Implementation of the concept in (A) using a pentagonal coupling slit carved in a gold layer, launching electromagnetic surface waves (SPPs) from each of its edges. (**C** and **D**) The amplitude, phase, and vector properties of the interference pattern are measured in two complementary ways: scattering scanning near-field optical microscopy (s-SNOM), which is time-averaged (C), and two-photon photoemission electron microscopy (2PPE-PEEM), which is time dependent (D). In s-SNOM, light is collected by scattering the near field with a sharp metallic tip, and in 2PPE-PEEM, electrons are emitted from the sample and used to image the near field through a short laser pulse arriving after the initial excitation. [See (36) for further explanations about the measurement methods.]
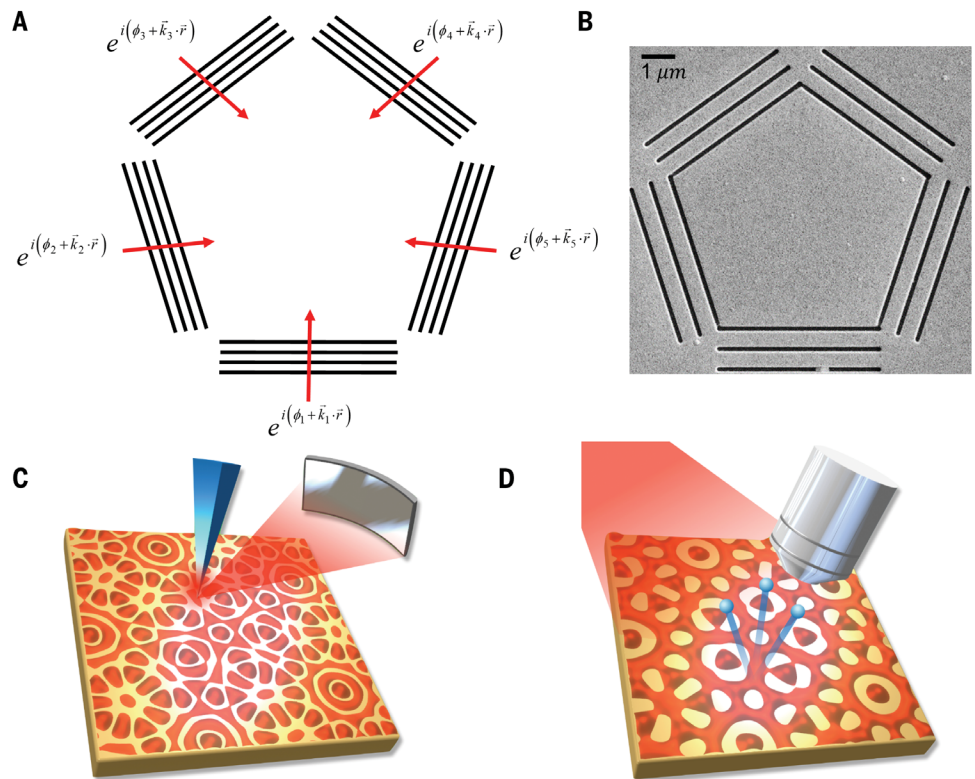
This representation is consistent with a periodic 4D space with elementary reciprocal vectors $\vec{g}_n = \left(\begin{bmatrix} \vec{k}_n \end{bmatrix}, \begin{bmatrix} \frac{\sin(2\pi/5)}{\sin(4\pi/5)} \vec{k}_{\mathrm{mod}(3n,5)} \end{bmatrix} \right)$ defining the higher-dimensional space (28, 36). Equation 2 illustrates the inherent higher dimensionality of quasicrystals and identifies the two ways to influence their topology: (i) by individually engineering the relative phases of waves comprising the crystal or (ii) by tuning their sum.

Identifying topological charge vectors in quasicrystals

From Eq. 2, it is clear that every configuration of relative phases φ_n will result in some dislocation vector in the 4D space, affecting the 2D projection of the quasicrystal (38, 39). For the specific choice $\phi_n = \frac{2\pi n Q}{5}, Q \in \{0, \pm 1, \pm 2\}$ we found, unexpectedly, that the resulting vectors $\vec{b}$ represent multidimensional topological charges, or topological charge vectors. Specifically, they adhere to a vector topological charge conservation law similar to that of other scalar systems (7, 40), which takes the form

$$\vec{b}_{Q_1} - \vec{b}_{Q_2} = \vec{b}_{Q_1 - Q_2} \qquad (3)$$

where $\vec{b}_{Q_1}, \vec{b}_{Q_2}, \vec{b}_{Q_2 - Q_1}$ are different topological charge vectors, found by assuming $\phi_n = \frac{2\pi n Q_1}{5}, \frac{2\pi n Q_2}{5}$, and $\frac{2\pi n (Q_1 - Q_2 - 5\lfloor(Q_1 - Q_2)/3\rfloor)}{5}$, respectively, in Eq. 2. Equation 3 is strictly fulfilled up to an elementary lattice vector in the emergent

periodic 4D space and has a cyclic dependence because of the finite number of solutions (40). See (36) for the full list of vectors fulfilling Eq. 3 and verification that it indeed persists. The vector $\vec{b}_{Q=0}$ is the trivial vector because there are only four nontrivial topological charge vectors according to Eq. 2, yet it is added for completeness of the point group symmetry of the system.

A similar requirement on the relative phases in a periodic or circular 2D system results in the existence of scalar topological charges, which are identified as phase singularities in the time-averaged wave interference pattern (40). These phase singularities have little meaning in the real-valued function of the crystal (Eq. 1), which is often used to define a charge distribution (27–29), but are immensely important in the analysis of waves (31). As we show experimentally below, such phase singularities are incapable of identifying the topology of the system for a quasicrystal, thus requiring the existence of topological charge vectors in the higher-dimensional space.

Although the topological charge vectors are 4D, they have only two nonzero components: one related to $\vec{b}_{phonon}$ and the physical 2D space topology and another related to $\vec{b}_{phason}$ and the topology in the two additional dimensions of the quasicrystal. This property, which stems from the two incommensurate length scales in our system (28, 29), greatly resembles the extension of the Chern number to a two-component

vector in the 4D quantum Hall effect with quasicrystals (25, 26).

4D topology of pentagonal plasmonic quasilattices

We explore the 4D topology described above by creating a pentagonal quasilattice of surface plasmon polaritons (SPPs) (41), electromagnetic surface waves existing at the interface between metallic and dielectric materials. For this, we used gold surfaces with pentagonal coupling slits nanofabricated through focused ion beam milling (Fig. 1D). Such a system exhibits the spin-orbit interaction of light (40), and similar designs were recently used to investigate a variety of nanophotonic topological charges (42, 43). The spin-orbit interaction of light determines the topological charge vector in the plasmonic quasilattice through a conservation law similar to Eq. 3 (36), where Q_1, Q_2 and $Q_2 - Q_1$ are replaced by physical constants related to the angular momentum of light, as in systems with the same SPP excitation mechanism (40, 44).

To fully characterize the topology, we used two complementary techniques: phase-resolved scattering scanning near-field optical microscopy (SNOM; Fig. 1E) (40, 42, 45) and time-resolved two-photon photoemission electron microscopy (2PPE-PEEM; Fig. 1F) (43, 46). 2PPE-PEEM is capable of recording the deep subcycle temporal evolution of the SPP quasilattice, which has a cycle time of a few femtoseconds,
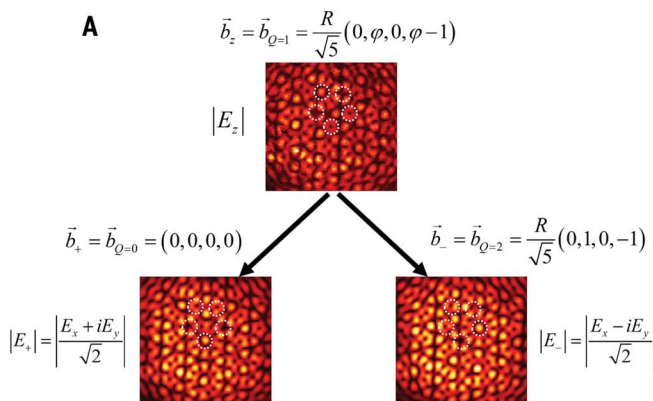
Fig. 2. Phase-resolved near-field microscopy of pentagonal plasmonic quasilattices. We showed that different pentagonal plasmonic quasilattices are not topologically distinct in 2D by examining their phase singularities. (**A** to **C**) Amplitude (A) and phase (B) of the out-of-plane field E_z of three different interference patterns of SPPs generated by impinging three different coupling slits with light carrying the same circular polarization (C). The positions of the edges making up the coupling slits were shifted to produce the required relative phases $\phi_n = \frac{2\pi nQ}{5}$ in Eq. 2, which generate the distinct topological charge vectors $\vec{b}_Q$ written above each panel in (C) [R is a characteristic length in the 4D space of the quasilattices, $\varphi = (1+\sqrt{5})/2$ is the golden ratio] (40). In each pattern, the central interference area, marked by a dashed circle in (A) and (B), shows the expected phase singularity from the relative phases, which should characterize the entire mode. By contrast, the solid circles in (B) show that all five possible phase singularities in 5-fold symmetry ($-2 \le q \le 2$) appear in each of the modes, albeit at different locations. One phase singularity is insufficient for characterizing the modes in their 2D representation, making them topologically indistinguishable in 2D. The imaged area is marked by a light square in each panel of (C), the location of which varies in accordance with the shifted position of the SPP interference pattern.


$$\vec{b}_{Q=0} = (0,0,0,0)$$

$$\vec{b}_{Q=-1} = \frac{R}{\sqrt{5}}(0,-\varphi,0,1-\varphi)$$

$$\vec{b}_{Q=2} = \frac{R}{\sqrt{5}}(0,1,0,-1)$$
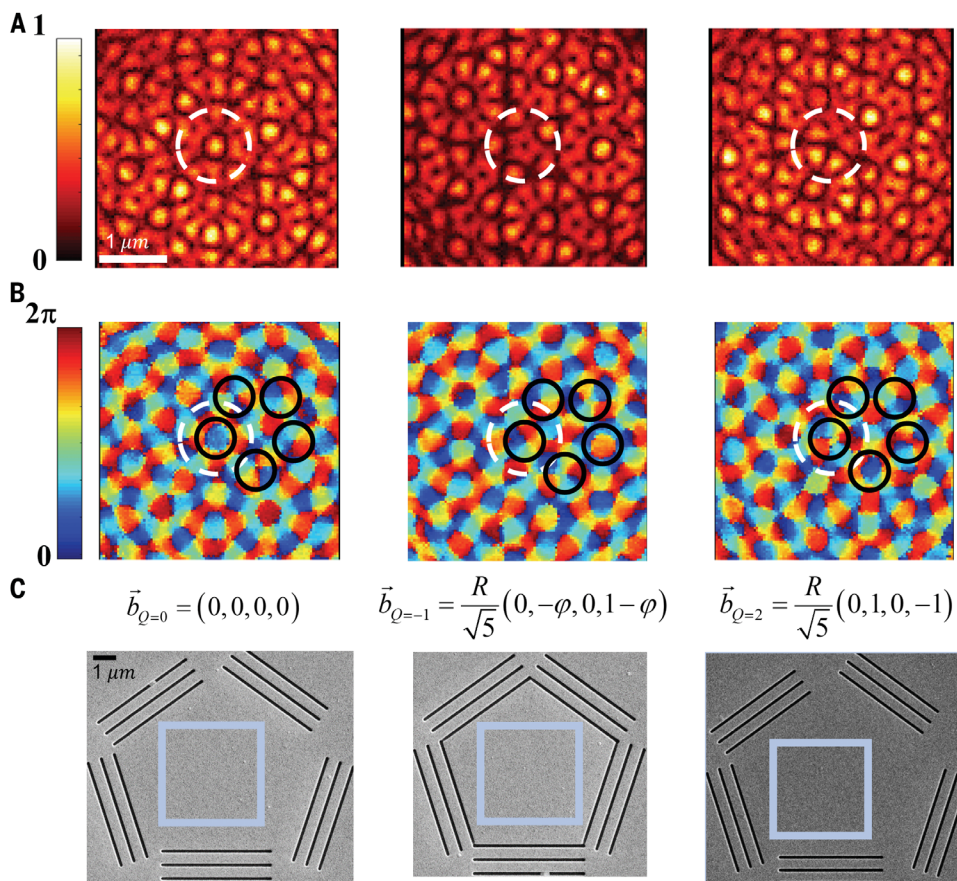
Fig. 3. Topological charge conservation in pentagonal plasmonic quasilattices.

(**A**) Measured amplitude of the out-of-plane electric field E_z, for a coupling slit with shifted edges such that $\phi_n = \frac{2\pi n}{N}$ ($Q = 1$). Because both amplitude and phase are extracted in the measurement, it is possible to reconstruct the two in-plane field components in the circular basis (E_+ and E_-) through Maxwell's equations (42). Whereas the out-of-plane field has a topological charge vector $\vec{b}_z$, the two in-plane field components have different topological charge vectors, $\vec{b}_+$ and $\vec{b}_-$, respectively. In the physical 2D plane, this manifests as

$$\vec{b}_z = \vec{b}_{Q=1} = \frac{R}{\sqrt{5}}(0,\varphi,0,\varphi-1)$$

$$|E_z|$$

$$\vec{b}_+ = \vec{b}_{Q=0} = (0,0,0,0)$$

$$\vec{b}_- = \vec{b}_{Q=2} = \frac{R}{\sqrt{5}}(0,1,0,-1)$$

$$|E_+| = \left|\frac{E_x + iE_y}{\sqrt{2}}\right|$$

$$|E_-| = \left|\frac{E_x - iE_y}{\sqrt{2}}\right|$$

a constant difference between the winding of every phase singularity for each field component (examples are marked in every panel by a dotted circle). (**B**) By choosing a different value of $\varphi_n = \frac{2\pi nQ}{N}$ through incident polarization or coupling slit design, a different set of topological charge vectors is generated. Conveniently, all topological charge vectors can be represented in the same plane, because for $\vec{b} = ([b_1, b_2], [b_3, b_4])$, only their b_2 and b_4 values are nonzero. Thus, the topological charge vectors of each mode form a triangle with a certain area. By performing a line integral through Stokes' law, keeping the direction of integration constant, and normalizing by the area of the projected 4D unit cell, the area of each triangle becomes exactly Q. Thus, topological charge conservation for vector pentagonal quasilattices is identical to an area law conservation.
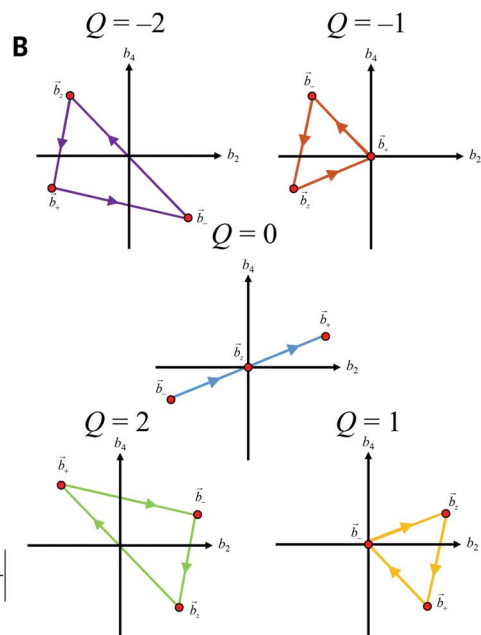
whereas SNOM provides time-averaged mapping of its amplitude and phase. Both methods have a sufficient deep-subwavelength spatial resolution.

The symmetry of the measured SPP field in both methods is different (as illustrated in Fig. 1, E and F): SNOM captures the time-averaged, complex field, exhibiting strictly pentagonal symmetry, whereas 2PPE-PEEM extracts the time-dependent, real part of the field, resulting in decagonal symmetry. Furthermore, SNOM captures the out-of-plane field component E_z, whereas in a pump-probe experiment involving SPPs, 2PPE-PEEM predominantly measures the in-plane field components E_x and E_y (47). Both methods, nevertheless, are capable of extracting the full vector field independently (42, 43). For more information about our various sample preparation and measurement protocols, see (36).

The time-averaged out-of-plane field measurements of pentagonal SPP quasilattices (Fig. 2, A and B) revealed that each lattice contains all possible phase singularities (i.e., $q = -2,-1,0,1,2$), albeit at different locations. Furthermore, as suggested in (29) and further investigated in (36), the lattices are locally isomorphic, meaning that a field pattern in one lattice can al-

ways be found in the others. Thus, the lattices appear to be topologically indistinguishable in 2D despite being distinguishable in 4D and having different topological charge vectors (displayed above each image in Fig. 2C).

In contrast to the purely scalar fields considered thus far, SPPs are composed of a 3D electric field (42, 43). Thus, each of the three field components is associated with a different topological charge vector determined by a conservation law articulated in (36). This conservation law is a direct result of Maxwell's equations, and relates the topology of the in-plane rotating fields (i.e., left-circular or right-circular) to the topology of the out-of-plane component. Therefore, 2D phase singularities around the same point appear with different windings in different field components, as demonstrated through time-averaged measurements and in accordance with the relation between their respective values of Q (Fig. 3A). Combined with topological indistinguishability in 2D, this unique vectorial trait changes the field orientation at any given position with time, effectively causing vector field features to disappear at one location and reappear in another (as demonstrated in movies S1 and S2).

Indistinct as it may be in 2D, the behavior of SPP quasilattices can be clearly understood in the 4D higher-dimensional space of quasicrystals, where the topological charge vectors of all field components form a triangle (Fig. 3B). A line integral surrounding the area of the triangle (i.e., using Stokes' law) gives exactly the value Q (36). Therefore, the vector nature of SPPs transforms the topological charge conservation in Eq. 3 into an area conservation law, holding true for any divergence-free vector field fulfilling similar relations to Maxwell's equations (48, 49).
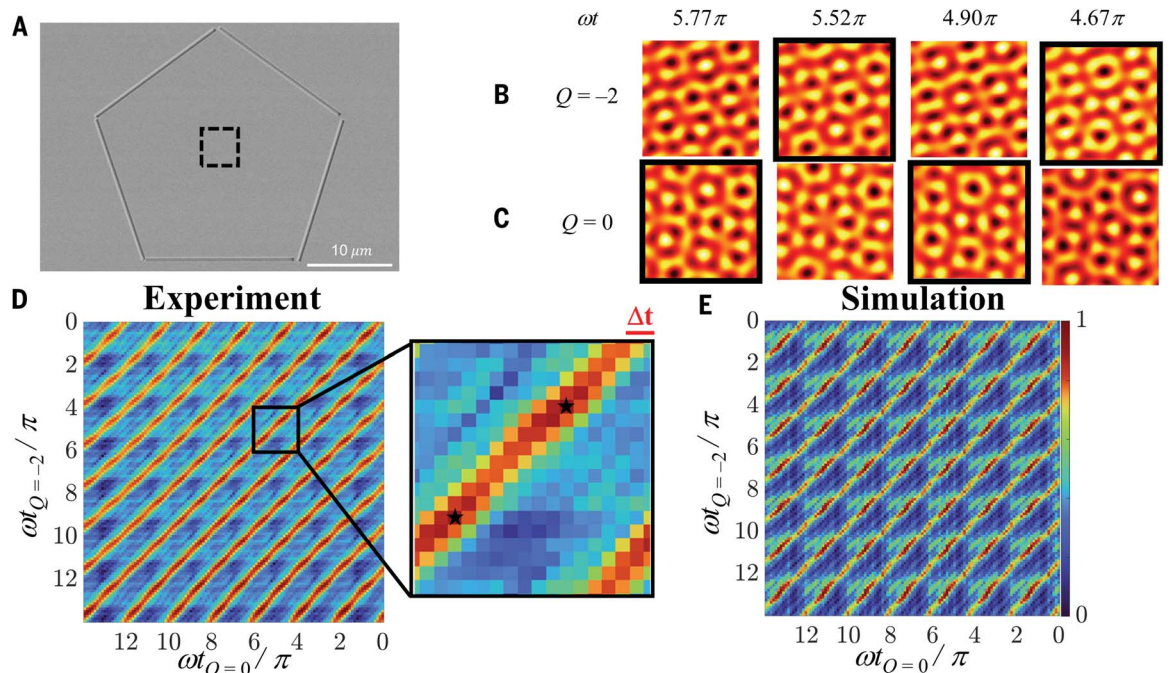
Controlling the 2D projection of plasmonic quasilattices with temporal phase

After exploring how the relative phases of the waves affect the topology of a quasicrystsal, we then investigated the influence of their sum. In doing so, we return to Eq. 1, noticing that it has the same functional form as the time-dependent solutions of the wave equation. Thus, one can write the relative phases ϕ_m of any monochromatic system satisfying the wave equation, e.g., electromagnetic, acoustic, etc., in the form $\phi_m = \alpha_m - \omega t$. Here, ω is the temporal frequency of the waves, t is the time coordinate, and α_m is the set of parameters tuning

Fig. 4. Controlling the 2D projection of topologically distinct quasilattices with the temporal phase. We verified that two plasmonic quasilattices are topologically distinct by measuring their temporal evolution, which exhibits similar patterns at different times. To this end, we examined two lattices generated by the same coupling slit. (**A**) SEM micrograph of the coupling slit used for the time-resolved measurement supporting two plasmonic quasilattices with relative phases $\phi_n = \frac{2\pi n Q}{5}$, $Q = 0,-2$, determined by changing the handedness of incident illumination.

(**B**) Real out-of-plane electric field of a quasilattice with $Q = -2$, extracted from a time-resolved PEEM experiment (51). The different accumulated temporal phase appears above every panel in (B). The dashed square in (A) marks the field area shown. (**C**) Same as (B) but with $Q = 0$. Similar field distributions are marked by bold frames and appear at different times for different quasilattices, as predicted. (**D** and **E**) Measured (D) and simulated (E) correlation between the two topologically distinct quasilattices as a function of their respective accumulated temporal phases. The vertical and horizontal axes represent the accumulated temporal phase of the field presented in (B) and (C), respectively. Inset in (D) shows a magnified region of the measurement times presented in (B) and (C), where the stars mark the coincidents of similar distributions indicated by the bold frames. The temporal distance between the similar distribution remains the same up to the temporal resolution of the measurement (manifesting in a phase error of ~0.125π) and is marked by Δt in the inset of (D). Color bar for both (D) and (E) is shown in the inset of (E) and represents the value of correlation between images of the two lattices at various times. The experimental correlation map in (D) greatly depends on the available field of view and the temporal resolution of the measurement. However, (E) shows that both effects can be accounted for by the simulation. Correlation without any such restrictions is given in fig. S2. The dynamics of the full vector field in (B) and (C) is given in movies S1 and S2, respectively.

the independent relative phases. For the choice of $\alpha_m = \frac{2\pi mQ}{5}$, Eq. 2 remains the same, but the sum of all relative phases Γ becomes exactly $-5\omega t$ (36). In this case, the topological charge vector does not change with Γ, which relates directly to the global time-dependent phase accumulation of the interference pattern. Instead, a constant phase factor is added to the interference, changing the 2D projection of the quasicrystal in time. Thus, whereas the time-averaged measurements of SPP quasilattices could not distinguish between lattices with a different topology, a time-dependent measurement can obtain the necessary information to do so.

A corresponding observation of this principle is presented in Fig. 4. We measured two topologically distinct SPP lattices at different times (examples are shown in Fig. 4, B and C) and correlated the time-resolved measurements as a function of the time difference (Fig. 4, D and E). We found that topologically distinct quasicrystals exhibited a similar real-space shape at different times [see (36) and fig. S2], and this time difference remained constant throughout their temporal evolution [see explanation in (36)]. Therefore, measuring the quasilattice at certain times allows one to select specific 2D projections and reveals the relationship between topological charge vectors of different quasilattices. Finally, understanding the topology of a quasicrystal made of interfering waves can only be complete once it is examined both in a time-averaged and a time-resolved manner.

Outlook

Our results prove the existence of topological charge vectors in the higher-dimensional space of 2D quasicrystals. The quasicrystal field distribution is a projection from higher-dimensional space and contains information about the higher-dimensional topology, which we monitored and controlled in a model experimental system: the interference of electromagnetic surface waves on gold. In principle, many of our results could be reproduced in other wave systems. Therefore, we conclude that quasicrystalline wave interference patterns are a simple and straightforward path to examine the topology of physical systems in higher dimensions.

Because of the pentagonal symmetry that we investigated, our topological charge vectors manifest in 4D. However, a higher prime-number symmetry provides more degrees of freedom and more nondegenerate topological charge vectors, scaling up the dimension of the examined topology. Additionally, it is possible that 3D topological defects such as skyrmions (42, 43) exist in our 2D quasicrystalline wave interference. Although skyrmion-like features appear (see movies S1 and S2), the boundary of a skyrmion is ill defined in our system, and thus they do not exist. Nevertheless, 4D spatiotemporal skyrmions were recently found to exist in time-modulated 3D quasicrystalline wave interference (50).

Figures 2 and 3 illustrate that the information contained within a quasicrystalline interference pattern is not local; that is, the correct characterization of its topological charge requires measuring the field in several locations. This property could benefit security protocols for the transport of both classical and quantum information (51) while making the information more resilient to noise and other interferences (52). Conversely, topological protection of the information could be achieved by producing quasicrystalline interference inside a nonlinear medium, creating nonlinear quasilattices (38, 39).

Although the model that we presented in Eqs. 1 to 3 is not system specific, it is heavily based on the model of interfering charge-density waves that has been used previously to explain the mechanical and thermodynamic properties of quasicrystalline materials (27–29). The correspondence between these models (36) suggests that the time-dependent phase accumulation of wave interference can be directly related to the variation of ground-state free energy in a given quasicrystalline material. Thus, our results shown in Fig. 4 provide a simulator exemplifying the way that free energy compensates for the presence of dislocations in a material. Further experiments can use this trait to examine the thermodynamics of quasicrystals under an adiabatic change in free energy, which is a very difficult task to perform by other means.

REFERENCES AND NOTES

1. T. W. B. Kibble, *J. Phys. Math. Gen.* **9**, 1387–1398 (1976).
2. J. F. Nye, M. V. Berry, *Proc. R. Soc. A Math. Phys. Eng. Sci.* **336**, 165–190 (1974).
3. M. König *et al.*, *Science* **318**, 766–770 (2007).
4. Z. Wang, Y. Chong, J. D. Joannopoulos, M. Soljačić, *Nature* **461**, 772–775 (2009).
5. J. M. Kosterlitz, D. J. Thouless, *J. Phys. C Solid State Phys.* **6**, 1181–1203 (1973).
6. H. N. S. Krishnamoorthy, Z. Jacob, E. Narimanov, I. Kretzschmar, V. M. Menon, *Science* **336**, 205–209 (2012).
7. D. J. Thouless, M. Kohmoto, M. P. Nightingale, M. Den Nijs, *Phys. Rev. Lett.* **49**, 405–408 (1982).
8. N. B. Simpson, K. Dholakia, L. Allen, M. J. Padgett, *Opt. Lett.* **22**, 52–54 (1997).
9. C. Wu *et al.*, *Sci. Adv.* **8**, eabk3075 (2022).
10. C. Nayak, S. H. Simon, A. Stern, M. Freedman, S. Das Sarma, *Rev. Mod. Phys.* **80**, 1083–1159 (2008).
11. G. Gibson *et al.*, *Opt. Express* **12**, 5448–5456 (2004).
12. S.-C. Zhang, J. Hu, *Science* **294**, 823–828 (2001).
13. W. A. Benalcazar, B. A. Bernevig, T. L. Hughes, *Science* **357**, 61–66 (2017).
14. J. B. Tai, I. I. Smalyukh, *Science* **365**, 1449–1453 (2019).
15. T. Bauer *et al.*, *Science* **347**, 964–966 (2015).
16. C. W. Peterson, W. A. Benalcazar, T. L. Hughes, G. Bahl, *Nature* **555**, 346–350 (2018).
17. M. Serra-Garcia *et al.*, *Nature* **555**, 342–345 (2018).
18. O. Boada, A. Celi, J. I. Latorre, M. Lewenstein, *Phys. Rev. Lett.* **108**, 133001 (2012).
19. K. Fang, Z. Yu, S. Fan, *Nat. Photonics* **6**, 782–787 (2012).
20. E. Lustig *et al.*, *Nature* **567**, 356–360 (2019).
21. L. Yuan, Q. Lin, M. Xiao, S. Fan, *Optica* **5**, 1396–1405 (2018).
22. D. Shechtman, I. Blech, D. Gratias, J. W. Cahn, *Phys. Rev. Lett.* **53**, 1951–1953 (1984).
23. D. Levine, P. J. Steinhardt, *Phys. Rev. Lett.* **53**, 2477–2480 (1984).
24. Y. E. Kraus, Y. Lahini, Z. Ringel, M. Verbin, O. Zilberberg, *Phys. Rev. Lett.* **109**, 106402 (2012).
25. M. Lohse, C. Schweizer, H. M. Price, O. Zilberberg, I. Bloch, *Nature* **553**, 55–58 (2018).
26. O. Zilberberg *et al.*, *Nature* **553**, 59–62 (2018).
27. P. Bak, *Phys. Rev. Lett.* **54**, 1517–1519 (1985).
28. D. Levine *et al.*, *Phys. Rev. Lett.* **54**, 1520–1523 (1985).
29. J. E. S. Socolar, T. C. Lubensky, P. J. Steinhardt, *Phys. Rev. B Condens. Matter* **34**, 3345–3360 (1986).
30. C.-K. Chiu, J. C. Y. Teo, A. P. Schnyder, S. Ryu, *Rev. Mod. Phys.* **88**, 035005 (2016).
31. N. D. Mermin, *Rev. Mod. Phys.* **51**, 591–648 (1979).
32. M. R. Dennis, K. O'Holleran, M. J. Padgett, *Prog. Opt.* **53**, 293–363 (2009).
33. F. M. Huang, Y. Chen, F. J. Garcia de Abajo, N. I. Zheludev, *J. Opt. A, Pure Appl. Opt.* **9**, S285–S288 (2007).
34. C. Rockstuhl, F. Lederer, T. Zentgraf, H. Giessen, *Appl. Phys. Lett.* **91**, 151109 (2007).
35. D. Pacifici, H. J. Lezec, L. A. Sweatlock, R. J. Walters, H. A. Atwater, *Opt. Express* **16**, 9222–9238 (2008).
36. See the supplementary materials for additional information.
37. J. M. Burgers, in *Selected Papers of J. M. Burgers* (Springer, 1995), pp. 335–389.
38. B. Freedman *et al.*, *Nature* **440**, 1166–1169 (2006).
39. B. Freedman, R. Lifshitz, J. W. Fleischer, M. Segev, *Nat. Mater.* **6**, 776–781 (2007).
40. S. Tsesses, K. Cohen, E. Ostrovsky, B. Gjonaj, G. Bartal, *Nano Lett.* **19**, 4010–4016 (2019).
41. S. A. Maier, *Plasmonics: Fundamentals and applications* (Springer, 2007).
42. S. Tsesses *et al.*, *Science* **361**, 993–996 (2018).
43. T. J. Davis *et al.*, *Science* **368**, eaba6415 (2020).
44. Y. Gorodetski, A. Niv, V. Kleiner, E. Hasman, *Phys. Rev. Lett.* **101**, 043903 (2008).
45. N. Ocelic, A. Huber, R. Hillenbrand, *Appl. Phys. Lett.* **89**, 101124 (2006).
46. G. Spektor *et al.*, *Science* **355**, 1187–1191 (2017).
47. D. Podbiel *et al.*, *Nano Lett.* **17**, 6569–6574 (2017).
48. H. Ge *et al.*, *Phys. Rev. Lett.* **127**, 144502 (2021).
49. K. Y. Bliokh, H. Punzmann, H. Xia, F. Nori, M. Shats, *Sci. Adv.* **8**, eabm1295 (2022).
50. D. Marco, M. A. Alonso, arXiv:2212.01366 (2022).
51. A. Sit *et al.*, *Optica* **4**, 1006–1010 (2017).
52. R. Zhang *et al.*, *Nat. Photonics* **15**, 743–750 (2021).

SUPPLEMENTARY MATERIALS

science.org/doi/10.1126/science.adt2495
Materials and Methods
Supplementary Text
Figs. S1 to S3
Table S1
References (53–57)
Movies S1 and S2

Submitted 18 September 2024; accepted 7 January 2025
10.1126/science.adt2495